International Journal of Heat and Mass Transfer 122 (2018) 59–68

Contents lists available at ScienceDirect

International Journal of Heat and Mass Transfer

journal homepage: www.elsevier.com/locate/ijhmt

Microscopic analysis of thin-film evaporation on spherical pore surfaces

Kimia Montazeri [a], Hyoungsoon Lee [b], Yoonjin Won [a,*]

[a] Mechanical and Aerospace Engineering, University of California, Irvine, CA 92697, USA
[b] School of Mechanical Engineering, Chung-Ang University, Seoul 06974, South Korea

ARTICLE INFO

Article history:
Received 6 October 2017
Received in revised form 26 December 2017
Accepted 2 January 2018

Keywords:
Copper inverse opals
Meniscus formation
Thin-film evaporation
Two-phase cooling

ABSTRACT

As electronic systems become miniaturized, it is crucial to implement optimal cooling technologies to dissipate high heat levels. Evaporation cooling for electronics systems has been considered one of the most promising approaches for meeting the demands of high-powered technologies by taking advantage of their latent heat. Integrating microscale or nanoscale features into two-phase microfluidic cooling systems such as porous media can dramatically increase the area of liquid-vapor interfaces where phonons translate thermal energy to fluid enthalpy. To achieve this performance jump, it is essential to understand how the engineered features improve evaporative heat transfer performance. In this study, we investigate thin-film evaporation performance within crystalline pore surfaces by employing simulation models that examine solid-liquid contact lines and liquid-vapor interfaces. The simulation models compute detailed performance parameters including phase volume fraction, temperature, pressure profile, and evaporative mass flux as a function of location, allowing us to calculate local heat transfer performance parameters. Based on local heat transfer performances, we identify thin-film regions and quantify their fractions to the overall evaporation performance. Area-averaged heat transfer coefficients are compared to identify the morphological effects of varying pore diameters and surface wettability. Insights from this parametric study will allow us to understand how evaporative heat transfer is related to the structural details of porous media and assist us to determine guidelines for the design of evaporating surfaces in modern electronics cooling.

1. Introduction

As electronic devices become smaller and more compact, their need for sophisticated and disruptive thermal technologies increases concomitantly [1]. Current thermal management solutions using air cooling [2], single-phase liquid cooling [3], or thermoelectric cooling schemes [4] cannot meet the demands of high-performance electronics, but two-phase cooling devices offer a promising approach over conventional single-phase cooling architectures by utilizing latent heat during the phase change process [5]. In particular, two-phase cooling devices integrating porous materials can significantly improve the evaporation region owing to their favorable combination of conduction and convection properties as well as their enormous interfacial area [6,7]. Porous materials provide conduction pathways through their solid fraction and enable efficient convection transport between solid and liquid phases through their large specific surface area. Therefore, the incorporation of porous materials into recent microfluidic heat exchangers such as vapor chambers and heat pipes [8] may push these devices to the fundamental limits of evaporative cooling. However, much more needs to be known about the relationship between porous materials' structural details and their evaporation performance before porous structures capable of pushing devices to their limits can be designed. Transport mechanisms in these materials present various design challenges. For example, liquid transport by capillary pumping within a porous medium competes with the viscous resistance associated with small pores [9–11]. Using engineered materials to control the shape of the meniscus and minimize diffusion lengths through the often-insulating liquid phase improves evaporation [12]. Most current challenges in the design of porous structures can eventually be overcome by performing theoretical parametric studies to identify the critical material parameters needed to engineer optimized evaporative cooling surfaces.

Recently, thin-film performances using nanoporous membranes [12,13] and microfabricated pin fin arrays [14] were experimentally investigated to explore the effects of morphological parameters (e.g., pore size, wick depth, and heated area) on evaporative heat transfer [15]. However, the ability of previous experiments to explain these phenomena has been limited by the structural materials and geometric parameters necessitated by their fabrica-

* Corresponding author.
E-mail address: won@uci.edu (Y. Won).

https://doi.org/10.1016/j.ijheatmasstransfer.2018.01.002
0017-9310/

Nomenclature

A	area, μm^2
C	Courant number
C_n	coefficients
CA	contact angle, °
c_p	specific heat, J/kg K
d	diameter, μm
E	energy, J/kg
g	gravitational acceleration, m/s^2
h_{fg}	enthalpy of evaporation, J/kg
k	thermal conductivity, W/m K
M	molar weight, kg/mol
$\dot{m}''$	mass flux, kg/m^2 s
N	number
P	pressure, Pa
q''	heat flux, W/m^2
Q	energy source, W/m^3
R	universal gas constant, J/mol K
r	radius, μm
S	volumetric mass source, kg/m^3 s
T	temperature, K
t	flow time, s
u	velocity, m/s

Greek symbols

α	volume fraction
δ	thickness, μm
μ	viscosity, Pa s
ρ	mass density, kg/m^3
σ	accommodation factor
ϕ	porosity

Subscripts

b	bottom
c	condensation
cell	cell
conv	convection
e or *evap*	evaporation
eff	effective
IO	inverse opal
in	in
l	liquid
lv	liquid-vapor
pore	pore
s	solid
sat	saturation
sl	solid-liquid
tf	thin film
v	vapor
via	via

tion methods [12], which requires a theoretical approach to attain a systematic parametric study. Furthermore, if evaporating surfaces are integrated with force convection flows, it is difficult to understand the flow effects of forced convection on evaporation without the aid of computational models [16]. Therefore, it is imperative to develop computational simulation models such as computational fluid dynamics (CFD) that allow to explore a wide range of parameters to complete the design guidelines or to carefully investigate the physics phenomena that are difficult to experimentally measure, particularly in the presence of nanoscale structures.

In this context, substantial efforts have been made to study phase change processes such as boiling [17,18], evaporation [19–24], and condensation [25,26] by implementing phase change theory into CFD simulation tools [27]. The wicking surfaces investigated in most prior studies include packed spheres [28–30], wire meshes [30], grooves [31–35], and sintered powder wicks [36] on the order of submillimeters [37]. The reported heat transfer coefficients in these studies are much lower than the theoretical limit based on kinetic theory because the effective thin-film area occupies only a small portion of the meniscus (approximately 10–20%), while most evaporative mass flux occurs through this small thin-film evaporating region [12,24,38,39]. This prior work motivates an examination of the local evaporation performance parameters of porous structures, in particular those sized on the order of tens of micrometers with the aim of investigating the role of structural characteristic lengths in determining thin-film evaporation performance.

To address such challenges, this study demonstrates a comprehensive analysis of the effects of microstructures on meniscus formation and thereby thin-film evaporation by employing highly-ordered porous materials. Here, we examine a wide range of morphological parameters by computing both solid-liquid contact lines and liquid-vapor interfaces in order to provide a set of guidelines for optimizing porous structures. The results of this study will allow us to pave the way to design better evaporating surfaces that effectively solve the thermal challenges posed by modern electronics devices.

2. Methods

2.1. Microstructure topology using inverse opals

This work investigates evaporative heat transfer parameters by studying copper inverse opals (IOs), a crystalline porous structure that possesses structural regularity, in order to understand the effects of morphology on evaporation performance. IOs are highly-ordered inverted structures of self-assembled sacrificial spheres forming a close-packed configuration (Fig. 1(a)) [40,41] The sacrificial spheres' diameter, ranging from 50 nm to 20 μm, determines pore diameter d_{pore}. After the sacrificial template is removed, the necks between adjacent spheres in the template will become "vias" (that is, interconnected windows between the pores), that enable high fluid accessibility with a large specific surface area. The manufacturing process for IOs precisely controls IOs' morphological parameters by modulating sacrificial sphere size, the annealing process, and the deposition material used. The combination of periodicity and regularity of IOs allows us to predict their physical transport parameters by developing a unit cell model with symmetry boundary conditions (Fig. 1(b)). In a prior study, we calculated the IOs' porosity and permeability assumed to be in a face-centered configuration (FCC), and the results showed a good agreement with experimental measurements [41].

2.2. Liquid meniscus computation

We track how liquid-vapor interfaces evolve within a spherical concave pore representing a unit cell of copper IO structures through Surface Evolver [42]. Surface Evolver solves for liquid-vapor interfaces associated with surface forces, the gravitational force, and other constraints (i.e., contact angle and volume) by cal-

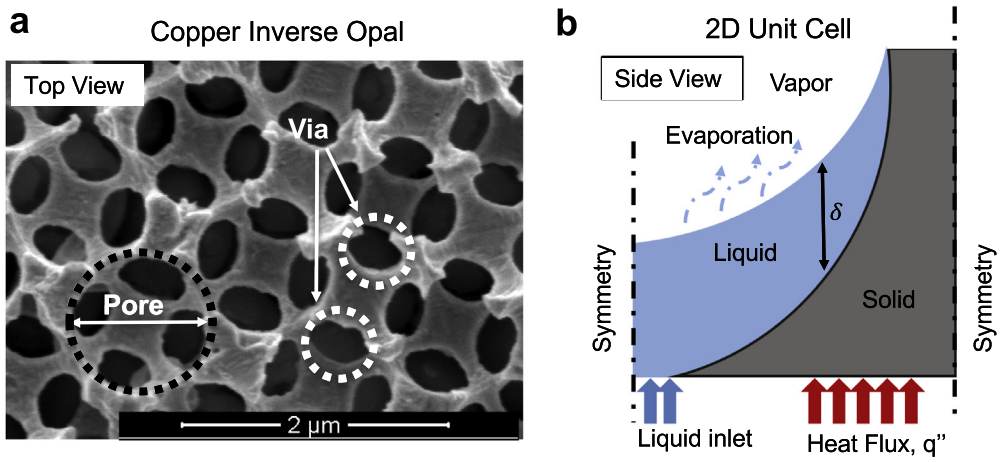

Fig. 1. The structural regularity and periodicity of copper inverse opals (IOs). (a) Representative scanning electronic microscope image of a copper IO structure showing face-centered configuration. The combined interconnectivity and periodicity of the pores provide liquid flow paths through the porous structure and enable a unit cell approach. (b) Schematic of the two-dimensional (2D) unit cell of IOs showing the symmetry boundary conditions. Liquid inlet with v = 0 m/s is introduced from the bottom liquid cells while a constant heat flux q″ is added to the bottom solid cells. In addition, the IOs' spherical concave shape helps to minimize meniscus thickness and to enhance evaporating areas.

culating the total energy for different conditions. The gradient descent method, a first-order iterative optimization algorithm, is used to find the local minimum of the total energy of interfacial surfaces. By repeating gradient descent iterations, the shape of liquid-vapor interfaces is obtained possessing the minimum total energy needed for the system reaches an equilibrium state. The liquid meniscus thickness for different contact angles inside an IO pore with a constant liquid volume fraction is shown in Fig. 2, where the normalized thickness is defined as the vertical distance between liquid-vapor and solid-liquid interfaces in an IO pore over the pore radius (see the vertical arrow in Fig. 1(b)). In this study, the volume of 32.5% of the IO pore will be filled with a liquid for the initial condition, which is the maximum liquid volume that maintains the liquid level below the centerline of the spherical IO pore for contact angles of 20–40°. As indicated, the liquid with smaller contact angles is prone to wet the IO pore surface, enabling

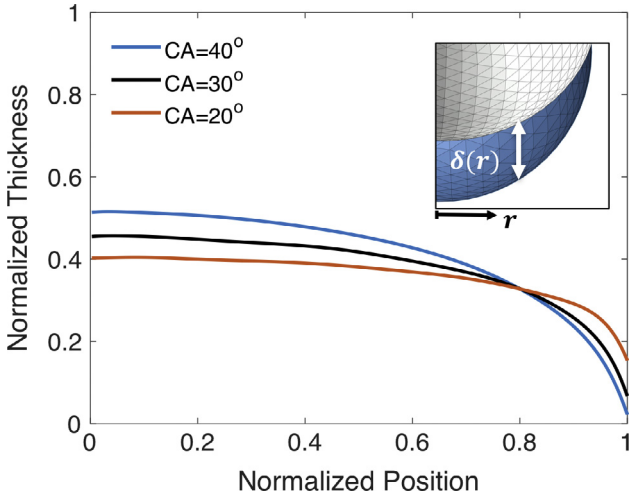

Fig. 2. Meniscus thickness as a function of position in the r-direction in normalized coordinates. Normalized thickness is calculated based on the ratio between the vertical distance between the liquid-vapor and solid-liquid lines and the pore radius. As a contact angle decreases, the thickness at the center decreases (where normalized r = 0) and the extended meniscus becomes larger. (Inset) Capture from Surface Evolver showing the interface between liquid (blue) and vapor (gray) phases in an IO pore (white). (For interpretation of the references to color in this figure legend, the reader is referred to the web version of this article.)

formation of an extremely thin liquid film over a larger area. In contrast, large contact angles lead to a thicker liquid film that occupies only a small portion of the IO pore surface. The meniscus shapes obtained from Surface Evolver are then imported into SolidWorks for post-processing, ANSYS Meshing for mesh generation, and ANSYS Fluent for CFD calculations, respectively.

3. Mathematical model

3.1. Governing equations

3.1.1. Volume of fluid method

Once the meniscus shapes are imported to ANSYS Fluent, volume of fluid (VOF) method identifies different phases to track liquid-vapor interfaces in the computational domain by assuming that the two phases do not interpenetrate each other. In the VOF method, a value of 1 indicates that the cell is filled with primary phase (liquid in this case) while a value of 0 indicates the cell is occupied by something other than the primary phase. Cells with values between 0 and 1 represent the presence of two-phase interfaces as Fig. 3 shows a representative phase contour. Afterwards, mass conservation equations are solved separately for liquid and vapor phases:

$$\frac{\partial}{\partial t}(\alpha_l \rho_l) + \nabla \cdot (\alpha_l \rho_l \vec{u}_l) = S_l \tag{1}$$

$$\frac{\partial}{\partial t}(\alpha_v \rho_v) + \nabla \cdot (\alpha_v \rho_v \vec{u}_v) = S_v \tag{2}$$

where α is the volume fraction, ρ is the density, u is the velocity vector, and S is the volumetric mass source term accounting for mass transfer between the phases. Subscripts l and v represent liquid and vapor, respectively. A single set of momentum and energy equations is solved for the entire domain:

$$\frac{\partial(\rho \vec{u})}{\partial t} + \nabla \cdot (\rho \vec{u}\,\vec{u}) = -\nabla P + \nabla \cdot [\mu(\nabla \vec{u} + \nabla \vec{u}^T)] + \rho \vec{g} + \vec{F} \tag{3}$$

$$\frac{\partial(\rho E)}{\partial t} + \nabla \cdot (\vec{u}(\rho E + P)) = \nabla \cdot (k \nabla T) + Q \tag{4}$$

where Q is the energy source term, and E is the energy, which can be defined as the phase-averaged value:

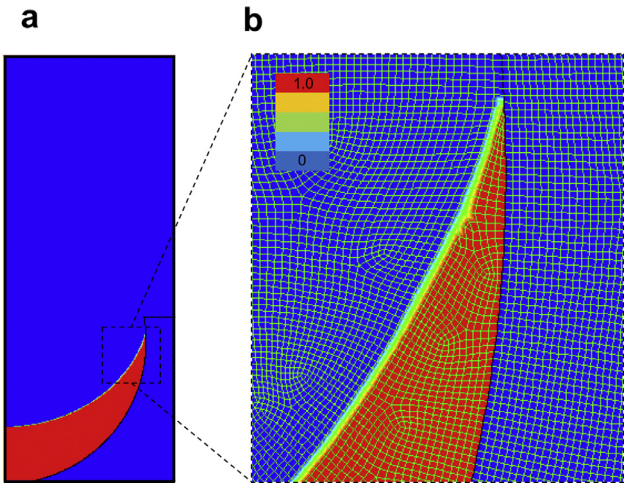

Fig. 3. Phase contour representing liquid and vapor phases on a solid surface. (a) Red (value of 1) indicates the liquid phase and blue (value of 0) indicates other phases. Cells with the values between 0 and 1 indicate vapor-liquid interfaces. (b) Close-up view of the phase contour showing the detailed mesh in different phases and at interface for the thin liquid film near the solid surface. (For interpretation of the references to color in this figure legend, the reader is referred to the web version of this article.)

$$E = \frac{\alpha_l \rho_l E_l + \alpha_v \rho_v E_v}{\alpha_l \rho_l + \alpha_v \rho_v} \tag{5}$$

The properties used in the momentum and energy equations are defined as effective values for the combined phase and are obtained based on the volume fractions of each phase:

$$\rho_{eff} = \alpha_l \rho_l + \alpha_v \rho_v \tag{6}$$

$$\mu_{eff} = \alpha_l \mu_l + \alpha_v \mu_v \tag{7}$$

$$k_{eff} = \alpha_l k_l + \alpha_v k_v \tag{8}$$

where μ is the viscosity, and k is the thermal conductivity.

3.1.2. Phase change at interfaces

The interfacial mass and energy transfer is considered by adding appropriate volumetric mass source term S and energy source term Q to the continuity and energy equations in Eq. (1), (2), (4), through the use of user-defined functions (UDFs). The volumetric mass source term imposed on the liquid phase S_l has a negative value because of the evaporative mass from liquid to vapor phase. Therefore, $S_l = -S_v = -\dot{m}''|\nabla \alpha_v|$ based on the Schrage model [43], where $|\nabla \alpha_v|$ is the interfacial area over the volume within one computational cell as expressed in this equation [41]:

$$|\nabla \alpha_v| = \frac{1}{V} \int |\nabla \alpha_v| dV = \frac{A_{lv,cell}}{V_{cell}} \tag{9}$$

The values of $|\nabla \alpha_v|$ are obtained by using a UDF to calculate evaporative mass fluxes. Then, an energy source term $Q = h_{fg} S_l$ is added to the energy equation at the liquid and vapor interfaces in order to account for the enthalpy difference between liquid and vapor during the phase change. Schrage theory [43] provides the correlation between the mass flux and the thermofluidic profiles in the two-phase system [26,45]:

$$\dot{m}'' = \frac{2}{2 - \sigma_c} \sqrt{\frac{M}{2\pi R}} \left[\frac{\sigma_c P_v}{\sqrt{T_v}} - \frac{\sigma_e P_l}{\sqrt{T_l}} \right] \tag{10}$$

where R is the universal gas constant (8.314 J/mol K), and M is the molar weight (0.018 kg/mol for water). In Eq. (10), the accommodation factor σ is the fraction of molecules transferred owing to the phase change while subscripts c and e dictate condensation and evaporation, respectively. In the most of previous studies, the accommodation factors for condensation σ_c and evaporation σ_e are treated as an identical value σ [44]. The value of $\sigma = 1$ means that all the molecules at the interface line changes their phases. Often, values larger than 0.1 are suggested for dynamic surfaces (i.e., boiling), and values smaller than 0.1 are suggested for static surfaces (i.e., condensation or evaporating surfaces) [45]. Tanasawa's model simplifies Eq. (10) by assuming that there is a small temperature jump between the liquid-vapor interface and vapor with a linear correlation between those two temperatures [46]:

$$\dot{m}'' = \frac{2\sigma}{2 - \sigma} \sqrt{\frac{M}{2\pi R}} \frac{\rho_v h_{fg} (T_{lv} - T_{sat})}{T_{sat}^{\frac{3}{2}}} \tag{11}$$

Tanasawa's assumption will be valid if there are small deviations $(T_{lv} - T_{sat})/T_{sat} \ll 1$ [47], which is the case for this study.

3.2. Numerical simulation

Based on the numerical correlations obtained Eqs. (1)–(10), transient thin-film evaporation models are developed to calculate thermofluidic performance parameters. First, a two-dimensional (2D) unit cell from Fig. 4(a) is considered by using incompressible and laminar flow with a pressure-based solver. The simulation models use semi-implicit method for pressure linked equations (the SIMPLE scheme) [48], least square cell-based formulation for gradient spatial discretization, and the PRESTO! scheme [49] for pressure discretization. In the model, the VOF method computes different phases with explicit formulation and implicit body forces while the volume fraction cutoff and the Courant number assume the default values of 10^{-6} and 0.25, respectively. High resolution interface-capturing (modified HRIC) [50] discretizes the volume fraction where its computational expense is smaller than the Geo-Reconstruct scheme. Momentum and energy equations are discretized using second-order upwind scheme [51]. Using the continuum surface force (CSF) model [52] helps to maintain constant contact angles during the evaporation process (see Table S1 for simulation details).

3.3. Geometry, boundary conditions, and material properties

This study examines a 2D IO unit cell for varying pore diameters from 10 μm to 20 μm. All the geometrical values are expressed as a function of pore diameter, such that geometrical values increase as pore diameter increases. Detailed dimension information for the unit cell is provided in Fig. 4(a). As boundary conditions for a 2D IO unit cell (with a width of $1.2r_{pore}$ and a height of $3r_{pore}$) are illustrated in Fig. 4(b), the working fluid is introduced through a via at a constant temperature with an inlet velocity of 0 m/s and a radius of the via ($r_{via} = 0.2r_{pore}$). The ratio between via and pore size yields a constant porosity of 78%. A heat flux of $q'' = 100$ W/cm^2 is applied to the solid portion of the bottom surface. The liquid in the inlet has a constant temperature of 373 K, and the solid phase is initially superheated at 380 K. We can track the recession of interface as the water evaporates inside the pore while the bubble nucleation on the solid-liquid interfaces is suppressed by using a UDF. Symmetric boundary conditions are applied at the sides because of the periodic structure of IOs. The pressure outlet boundary condition is used at the top surface, and the temperature at the outlet is equal to the vapor saturation temperature T_{sat}. In all simulation models, the working fluid and the solid material are water and copper, respectively. The thermophysical properties of water and copper are listed in Table S2 and S3 where saturation temperature and enthalpy of evaporation are reported at a pressure of 1 atm.

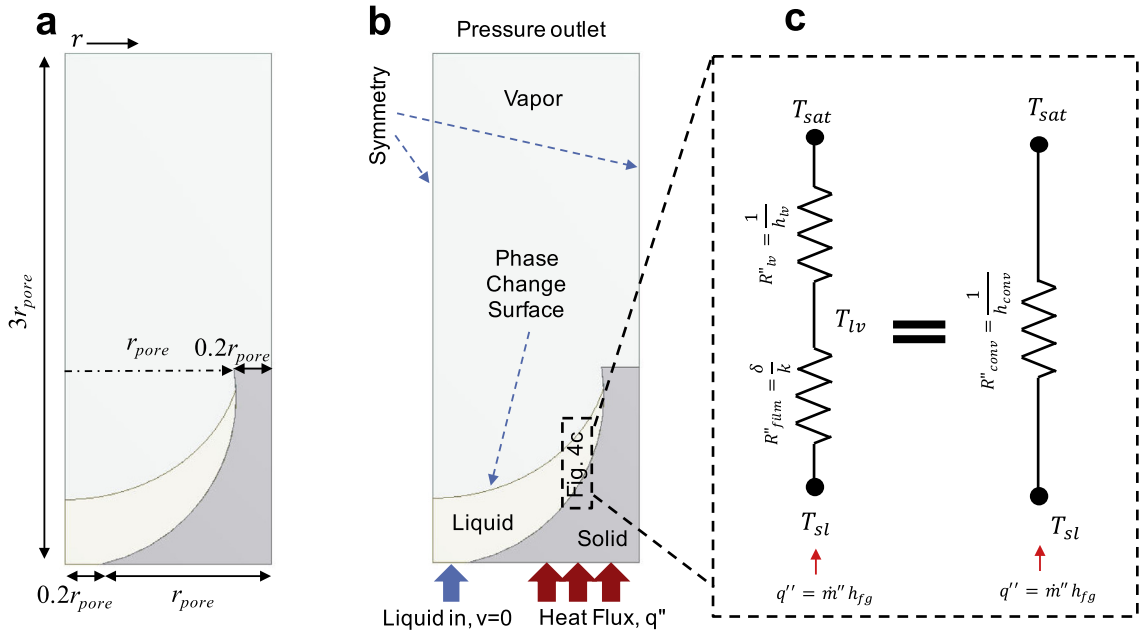

Fig. 4. Computational unit cell of copper IO showing geometrical details and boundary conditions. (a) Unit cell dimensions are indicated where the via is defined as 20% of a pore diameter. (b) Boundary conditions include liquid in and a constant heat flux in from the bottom surface as well as symmetry conditions due to the periodicity of the IOs. Liquid to vapor phase change occurs only at the interfacial regions. (c) Thermal circuits represent the film resistance and interfacial transport resistance in series (left), which is equivalent to the convective heat transfer resistance (right) based on the one-dimensional conduction assumption.

4. Results

We perform a parametric study of evaporation performance by testing various pore diameters of copper IO cells ranging from 10 to 20 μm and contact angles of 20° to 40°. The computational models directly provide thermofluidic parameters such as spatial and temporal temperatures, pressures, velocity profiles, and evaporative mass fluxes, allowing us to compute heat transfer coefficients. The thermofluidic parameters are collected and reported in this work once the interfacial parameters get stabilized after 10 to 20 μs for different cases (see Fig. S4).

4.1. Local evaporative mass flux

The computational simulation models calculate local evaporative mass flux using the simplified version of the Schrage model expressed in Eq. (11). Evaporative mass flux is plotted for pore diameters of 10 μm and 20 μm in Fig. S1(a) and (b).

4.2. Temperature profiles

Fig. 5(a) shows the temperature contour in the liquid, vapor, and solid domains of the evaporating meniscus where pore diameter is 10 μm and the contact angle is 20°. Fig. 5(b) shows the plot of the detailed temperature profile $T_{lv}(r)$ along the liquid and vapor interface (liquid volume fraction = 0.5) under steady-state conditions. As indicated, the temperature T_{lv} is minimum at the center of the pore (at $r = 0$ μm), and this value is influenced by the liquid inlet with a constant temperature of 373 K. The temperature T_{lv} near the wall (at $r = r_{pore}$ μm) is shown to be much higher because of lower conduction resistance through the liquid film, which is proportional to liquid film thickness based on Fourier's conduction law.

In the solid region of the unit cell, the conduction is the dominant heat transfer mode. Therefore, the temperature deviation is relatively small (compared to temperature profiles in the liquid or vapor regions) because copper has a high thermal conductivity. The local temperature information $T_{sl}(r)$ is plugged into Eq. (12) to calculate the corresponding local heat transfer coefficient. The area-averaged solid temperatures T_{sl} for different pore diameters and contact angles are compared in Fig. 6. In this plot, as pore diameter increases, average temperature increases as well. This might be evidence of efficient evaporation performance for smaller pore diameters.

4.3. Computation of local heat transfer coefficient

To characterize the evaporative heat transfer performance in a copper IO cell, we assume one-dimensional (1D) heat transfer [53] from the solid surface to the liquid (phonons and electrons in solid phase translate thermal energy to fluid enthalpy) and from the liquid to the evaporating surface (thermal energy is transferred by both conduction and advection through the thin-film liquid region and further translated through to the vapor region via thin-film evaporation). Such transport physics with a 1D assumption can be represented by the thermal resistances in series in Fig. 4(c). The heat flux $q'' = h_{conv}(r)(T_{sl}(r) - T_{sat})$ is assumed to be equal to the heat flux transferred through the interface $q'' = \dot{m}''(r)h_{fg}$. Therefore, the local heat transfer coefficient can be calculated as:

$$h_{conv}(r) = \frac{\dot{m}''(r)h_{fg}}{T_{sl}(r) - T_{sat}} \tag{12}$$

by using local evaporative mass flux $\dot{m}''(r)$ and local solid-liquid temperature $T_{sl}(r)$. In Fig. 4(c), the combined thin-film resistance and evaporation resistance can be defined as the local convective thermal resistance $R_{conv}(r)$:

$$R_{conv}(r) = \frac{1}{h_{conv}(r)A} \tag{13}$$

where A is the heat transfer area.

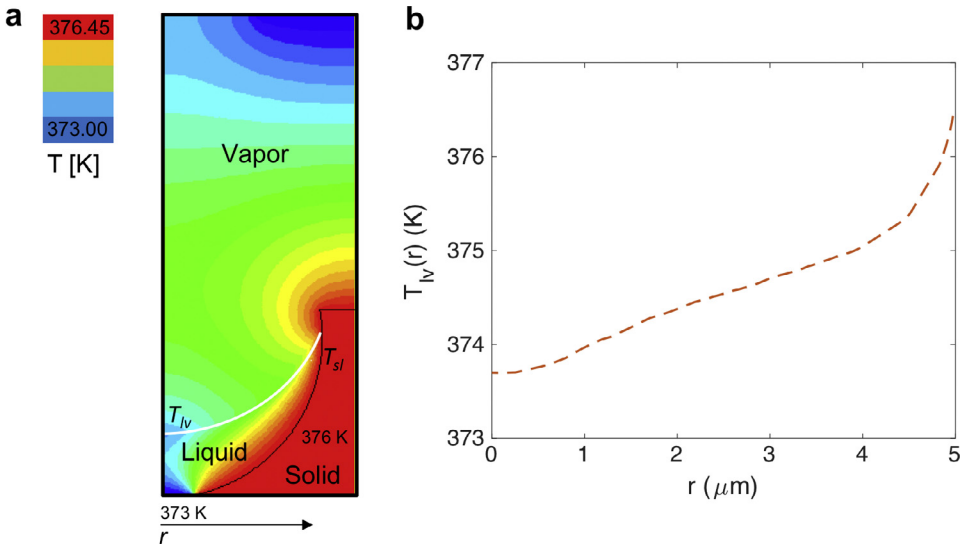

Fig. 5. Temperature profile of the liquid, vapor, and solid domains under evaporation regions where d_{pore} = 10 μm and CA = 20°. (a) Temperature contour showing the increase in temperature at the wall along the interface. (b) Temperature profile along the liquid-vapor interface is plotted against the r-axis, confirming lower temperature at the inlet and higher temperature near the wall at r = 5 μm.

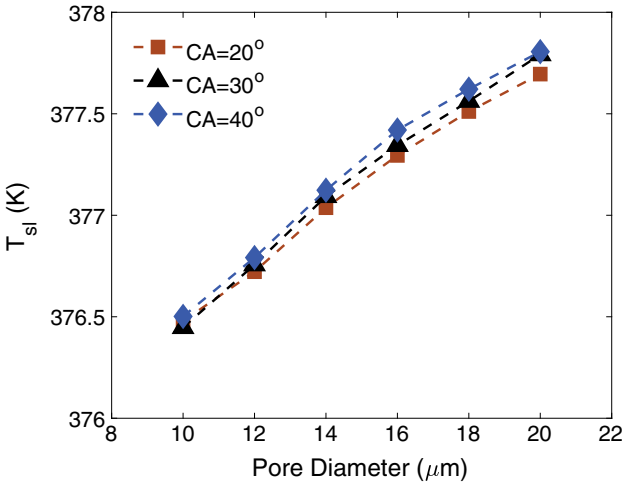

Fig. 6. Area-averaged temperature of solid-liquid contact lines for varying pore diameters and CA = 20°. As the pore diameter increases, solid temperature increases, indicating decreased evaporation rates.

In this work, the local convective heat transfer coefficient along the interface is computed as a function of the radius, which allows us to understand the local evaporative heat transfer performance related to local meniscus thickness. Fig. 7 shows the representative $h_{conv}(r)$ profiles using copper IOs with pore diameters of 10 μm and 20 μm. In this plot, a maximum h_{conv} at the wall increases to the values of 700 kW/m^2 K in the thin-film region for both cases. This heat transfer coefficient shows a good agreement with the existing data in the literature ranging from 800 to 1000 kW/m^2 K [29] testing copper microstructures with the characteristic lengths of 10–100 μm using CFD simulations, and these values are higher than experimental values [14].

5. Discussion

This study computes local and average heat transfer coefficients to reveal the crystalline IOs' role in improving thin-film evaporation as it relates to meniscus shapes. Local heat transfer coefficients are calculated based on the local evaporative mass flux and the difference between the solid-liquid temperature and the saturation temperature, and they are used to identify different evaporation regions along the interface. The area-averaged heat transfer coefficients are computed to compare overall evaporative heat transfer performance for a variety of cases.

5.1. Evaporation region identification

Fig. 7 and Fig. S1 show plots of local evaporation performance parameters, based on the modified Schrage model. In these plots, the local evaporative mass flux and local heat transfer coefficients are roughly inversely proportional to the local meniscus thickness. Based on these plots, three main evaporation regions can be identified: a thin-film region, a transition region, and a non-effective region as a function of the radial location as illustrated in Fig. 7. (1) The **thin-film region** ($0.9r_{pore} < r < r_{pore}$), the most efficient of the three regions, occurs near the wall where a sudden decrease in thin-film thickness is observed [30]. The thin-film region occupies only a small portion of the thin meniscus, but a large portion of evaporation occurs through this small region. In order to account for the thin-film effects, it is necessary to quantify the ratio of evaporative mass transfer through the thin-film area (in the range of $0.9r_{pore} < r < r_{pore}$) to the total evaporative mass transfer through the entire interface, which is called the "fraction" of the thin-film region:

$$fraction_{tf} = \frac{\int_{0.9r_{pore}}^{r_{pore}} \dot{m}'' dr}{\int_{0}^{r_{pore}} \dot{m}'' dr} \tag{14}$$

In Fig. 8(a), the fraction of thin-film evaporation to the total evaporation is plotted for varying pore diameters, which ranges from 28% to 53% as pore diameter increases from 10 to 20 μm. Smaller pores show smaller fractions, indicating the creation of efficient and uniform evaporation over the pore surface but larger heat transfer coefficients over the thin film (Fig. 8(b)). Larger pores show larger fractions because the evaporation of larger pores is dominated by the presence of a thin-film region. (2) The **transition region**, the transition between the thin-film region and the non-effective region, occupies a large portion of the meniscus. (3) In the **non-effective region** (if a local evaporative mass flux is less than 1% of the maximum evaporative mass flux), the local temper-

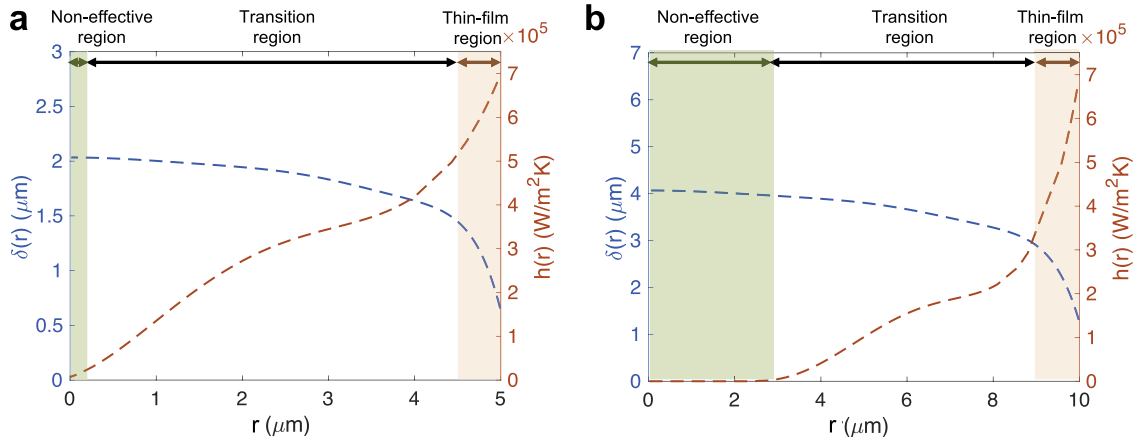

Fig. 7. Local meniscus thickness and time-averaged heat transfer coefficient along the liquid-vapor interface under steady-state conditions are shown for (a) d_{pore} = 10 μm and (b) d_{pore} = 20 μm where CA = 20°. Based on these local plots, three evaporation regions are identified: a thin-film region ($0.9r_{pore} < r < r_{pore}$), a transition region, and a non-effective region.

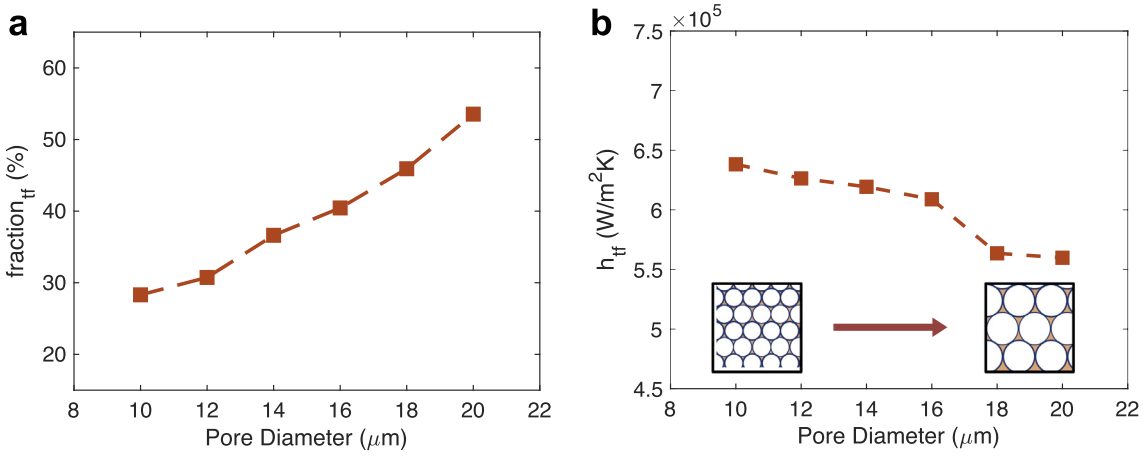

Fig. 8. Evaporation parameters of thin-film region for varying pore diameters. (a) Fraction of evaporation in the thin-film region to the total area. (b) Area-averaged heat transfer coefficient over the thin-film region. Smaller pores show smaller fractions but larger heat transfer coefficients, indicating the creation of efficient and stable evaporation while the evaporation of larger pores is dominated by the thin-film region only.

ature profile is directly affected by the inlet temperature, which is often lower than the saturation temperature. Thereby, evaporation occurs at a very slow rate.

5.2. Effects of pore diameters on evaporation

In order to understand the impact of different pore diameters on overall evaporation performance, area-averaged evaporative mass flux, evaporative heat flux, and convective heat transfer coefficients as a function of pore diameter are calculated in Fig. 9 and Fig. S2. In Fig. 9(a) and (b), decreasing the pore diameter from 20 μm to 10 μm increases the convective heat transfer coefficient by ~60% and area-averaged evaporative mass flux by ~15%. The fitting lines estimate the area-averaged convective heat transfer coefficients by using following correlation: $h = C_1 d_{pore} + C_2$ (W/m^2 K) where C_1 is $-13{,}330 \times 10^6$ W/m^3 K and C_2 is 520,290, 483,560, and 460,130 W/m^2 K for CA = 20°, 30°, and 40°, respectively. The trend can be attributed to the presence of different portions of non-effective regions for different pore diameters, as is compared in Fig. 7. For example, local region plots indicate that a smaller pore diameter (d_{pore} = 10 μm) demonstrates a small portion of a non-effective region (<5%) while a larger pore diameter (d_{pore} = 20 μm) shows a large portion of a non-effective region (30%), which helps small pores to enable more efficient evaporation in overall. The total heat transfer rate can be directly calculated as $q_{evap} = q''_{evap} A_{lv}$. In this equation, the total area of the evaporating surface is proportional to the single pore's surface area and the number of pores: $A_{lv} = A_{pore} N_{pore}$ where N_{pore} is inversely proportional to A_{pore}, providing a constant evaporating surface area for different pore sizes. Therefore, this investigation concludes that attaining small characteristic lengths and corresponding large heat transfer coefficients is critical to enhancing evaporation performance in crystalline porous structures.

5.3. Role of contact angles in evaporation

In addition to pore diameters, another important parameter determining overall evaporation performance is surface wettability, which can be quantified with a contact angle. Often, surface wettability can be controlled by surface engineering methods that modulate surface roughness and chemistry. In order to account for such surface engineering effects, we vary the contact angles between the solid wall and the liquid inside the pore by 20° to 40° in our simulation models. The contact angle values are directly plugged into Surface Evolver to determine the liquid film thickness first and then the thermofluidic properties of simulation domains

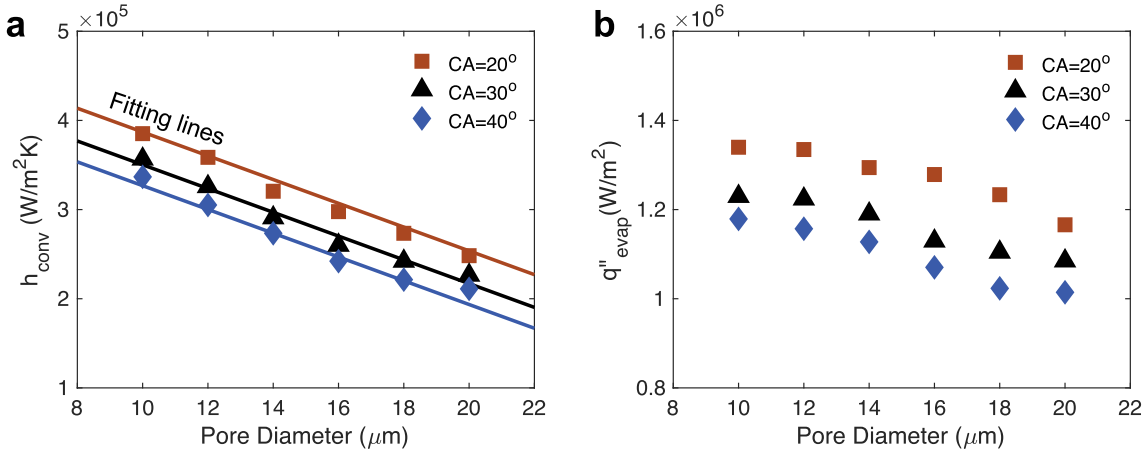

Fig. 9. Area-averaged evaporation performance values for varying pore diameters and contact angles. (a) Area-averaged heat transfer coefficient and (b) heat flux are plotted for different cases. Changes in pore diameters and contact angles will significantly affect the corresponding heat transfer coefficients. Fitting lines can estimate the area-averaged heat transfer coefficients in (a).

are calculated using the CFD models (see Sections 3 and 4). Surface wettability plays key roles in determining evaporation performance parameters: Liquid with smaller contact angles (1) is prone to wet IO surfaces, allowing creating enormous evaporating surfaces; (2) minimizes the thickness deviation along the interface, enabling more stable evaporating performance over the entire system; and (3) results in efficient evaporation properties (Fig. 9). As a result, as contact angle decreases from 40° to 20°, the improvement in evaporation is reported as ~15%.

6. Validation of the computational model

6.1. Mesh independence study

The Courant number indicates the numerical correlations among the computational cell size Δx, the transient time step Δt, and the velocity of the liquid flowing inside the cell v, as in $C = v\Delta T/\Delta x$. The Courant number thus explains how much information propagates through a computational cell at each time step and directly affects the convergence quality of the calculations. Using inappropriate values of Courant number results in data transfer through more than one cell at each time step, causing a calculation to be unstable and unphysical [51]. Considering the microscale computational domain of a single unit cell, to maintain the Courant number within convergence criteria (the Courant number is usually smaller than 1 in the VOF method), a time step vale of 10^{-9} s is required. Based on this time step, it is essential to choose a mesh size that allows a reasonable calculation time for the simulation process. To confirm the independence of the results from the computational mesh of this work, we test three different mesh sizes via numerical simulations. The number of cells in mesh 1, mesh 2, and mesh 3 is 9151, 36,579, and 145,019, respectively. The average size of mesh 1, mesh 2, and mesh 3 is 0.112, 0.054, and 0.024 μm, respectively. Temperature profiles along the liquid-vapor interface and the solid-liquid contact line are calculated for each of the meshes and are listed in Table S4. The percentage differences between the average wall temperature and the interface temperature for pairs of meshes are calculated in Table S5. Since the deviations between the results are negligible, we choose to use mesh 2 as the discretized domain for our simulations.

6.2. Mass balance calculation

In order to prove the simulation calculations' accuracy, the mass conservation is confirmed by calculating the evaporative mass flux from the liquid-vapor interface and the mass flux leaving the system, which shows errors consistently smaller than 11% as shown in Fig. S5. These errors are attributed to the presence of the evaporation rate in adjacent cells to the interface that are not included in the definition of the liquid-vapor interface line.

6.3. Limitation of CFD models

CFD computations are challenging because phase change models predominantly rely on the rough estimation of empirical values (i.e., accommodation factors [52]). This work uses a value of 0.1 for the accommodation factor; this value is widely used in previous literatures dealing with evaporation phenomena [53]. Furthermore, CFD computations are suitable for microscale systems but not ideal for nanoscale calculations whereas atomistic-level calculations are capable of calculating individual particle behaviors and their interactions based on numerical algorithms that account for interatomic forces between particles. For example, as pore diameter decreases to 1 μm, the meniscus thickness decreases to an order of nanometers. In this case, the atomistic-level calculations that account for intermolecular forces between water and copper molecules might be more critical and should be considered. Also, disjoining pressure—the excess pressure required for evaporation in the thin-film region owing to the presence of solid-liquid interactions—is significant in small-scale evaporation [11,35]. However, the effects of disjoining pressure on the suppression of evaporation could not be considered in the present work without considering the effects of intermolecular forces in the thin-film region on the evaporation process. Furthermore, interfacial temperature jumps cannot always be neglected in microscale simulations [47]. Therefore, in order to capture more complex phase change physics at interfaces, atomistic-level calculations might be considered as a follow up study.

7. Conclusion

This study investigates the effects of pore surfaces on meniscus formation and evaporation parameters by computing both solid-liquid contact lines and liquid-vapor interfaces with the aim of understanding evaporation through the use of a crystalline porous structure composed of inverse opals. A liquid meniscus shape is defined based on the minimum total surface free energy for a given intrinsic contact angle and imported as an initial condition for two-phase calculations. The two-phase models compute transient thermofluidic properties such as local temperature, pressure, phase

volume fractions, and mass flux by tracking liquid-vapor interface changes, allowing us to evaluate local heat transfer coefficients along the interface for varying cases. The local convective heat transfer coefficients increase as the meniscus thickness decreased, to a maximum value of 700 kW/m^2 K near the wall. This analysis identifies how thin-film regions occupying a small portion of the overall interface area dominate the total evaporation rate for larger pores whereas smaller pores create efficient evaporation over the entire pore. Correlating area-averaged convective heat transfer coefficients to pore diameters and contact angles reveals that decreasing pore diameter from 20 μm to 10 μm improves the evaporative heat transfer coefficient by up to ~60% and that decreasing contact angle from 40° to 20° improves the evaporative heat transfer coefficient by ~15%. These results suggest that incorporating smaller pores with desirable surface engineering will create improved hydrophilic surfaces that enhance evaporation performance. The fundamental insights from this study will enable rational design of evaporating surfaces to address thermal challenges in many applications.

Conflict of interest

Authors declare that there is no conflict of interest.

Acknowledgement

This work was sponsored by the National Science Foundation (NSF) – United States, (CBET-TTP 1643347, Dr. Jose Lage, the Program Director, Thermal Transport Processes) and the National Research Foundation of Korea (NRF) grant funded by the Korea government (Ministry of Science, ICT & Future Planning) (No. 2017R1C1B5017566). K.M. is thankful for the financial support from the UCI Mechanical and Aerospace Engineering Department Graduate Fellowship.

Appendix A. Supplementary material

Supplementary data associated with this article can be found, in the online version, at https://doi.org/10.1016/j.ijheatmasstransfer.2018.01.002.

References

[1] R.J. McGlen, R. Jachuck, S. Lin, Integrated thermal management techniques for high power electronic devices, Appl. Therm. Eng. 24 (8) (2004) 1143–1156, https://doi.org/10.1016/j.applthermaleng.2003.12.029.
[2] H.Y. Zhang, D. Pinjala, P.S. Teo, Thermal management of high power dissipation electronic packages: From air cooling to liquid cooling, in: Electronics Packaging Technology, 2003 5th Conference (EPTC 2003), IEEE, 2003, pp. 620–625. 10.1109/EPTC.2003.1271593.
[3] A. Heydari, Sun Microsystems, Inc., Multiple component field-replaceable active integrated liquid pump heat sink module for thermal management of electronic components. U.S. Patent 7,219,714, 2007.
[4] J.W. Vandersande, J.P. Fleurial, Thermal management of power electronics using thermoelectric coolers, in: Thermoelectrics, 1996., Fifteenth International Conference on, IEEE, 1996, pp. 252–255. 10.1109/ICT.1996.553311.
[5] Carey, V.P., 1992. Liquid-vapor phase-change phenomena.
[6] L.A. Richards, Capillary conduction of liquids through porous mediums, Physics 1 (5) (1931) 318–333.
[7] J.W. Palko, H. Lee, C. Zhang, T.J. Dusseault, T. Maitra, Y. Won, D.D. Agonafer, J. Moss, F. Houshmand, G. Rong, J.D. Wilbur, D. Rockosi, I. Mykyta, D. Resler, D. Altman, M. Asheghi, J.G. Santiago, K.E. Goodson, Extreme convective boiling from template-fabricated microporous copper on laser-etched diamond, Adv. Funct. Mater. 27 (2017) 1703265, https://doi.org/10.1002/adfm.201703265.
[8] B.D. Iverson, T.W. Davis, S.V. Garimella, M.T. North, S.S. Kang, Heat and mass transport in heat pipe wick structures, J. Thermophys Heat Transf. 21 (2) (2007) 392–404.
[9] L.A. Slobozhanin, J.I.D. Alexander, S.H. Collicott, S.R. Gonzalez, Capillary pressure of a liquid in a layer of close-packed uniform spheres, Phys. Fluids 18 (8) (2006) 082104, https://doi.org/10.1063/1.2236123.
[10] S. Prager, Viscous flow through porous media, Phys. Fluids 4 (12) (1961) 1477–1482, https://doi.org/10.1063/1.1706246.
[11] S. Narayanan, A.G. Fedorov, Y.K. Joshi, Interfacial transport of evaporating water confined in nanopores, Langmuir 27 (17) (2011) 10666–10676, https://doi.org/10.1021/la201807a.
[12] R. Xiao, S.C. Maroo, E.N. Wang, Negative pressures in nanoporous membranes for thin film evaporation, Appl. Phys. Lett. 102 (12) (2013) 123103, https://doi.org/10.1063/1.4798243.
[13] D.F. Hanks, Z. Lu, S. Narayanan, K.R. Bagnall, R. Raj, R. Xiao, R. Enright, E.N. Wang, Nanoporous evaporative device for advanced electronics thermal management, in: Thermal and Thermomechanical Phenomena in Electronic Systems (ITherm), 2014 IEEE Intersociety Conference on, IEEE, 2014, pp. 290–295. 10.1109/ITHERM.2014.6892295.
[14] D. Ćoso, V. Srinivasan, M.C. Lu, J.Y. Chang, A. Majumdar, Enhanced heat transfer in biporous wicks in the thin liquid film evaporation and boiling regimes, J. Heat Transf. 134 (10) (2012) 101501, https://doi.org/10.1115/1.4006106.
[15] S. Adera, D. Antao, R. Raj, E.N. Wang, Design of micropillar wicks for thin-film evaporation, Int. J. Heat Mass Transf. 101 (2016) 280–294, https://doi.org/10.1016/j.ijheatmasstransfer.2016.04.107.
[16] S. Narayanan, A.G. Fedorov, Y.K. Joshi, Experimental characterization of a micro-scale thin film evaporative cooling device, in: Thermal and Thermomechanical Phenomena in Electronic Systems (ITherm), 2010 12th IEEE Intersociety Conference on, IEEE, 2010, pp. 1–10. 10.1109/ITHERM.2010.5501327.
[17] J.Y. Chang, S.M. You, Boiling heat transfer phenomena from microporous and porous surfaces in saturated FC-72, Int. J. Heat Mass Transf. 40 (18) (1997) 4437–4447, https://doi.org/10.1016/S0017-9310(97)00055-0.
[18] C. Li, G.P. Peterson, Parametric study of pool boiling on horizontal highly conductive microporous coated surfaces, J. Heat Transf. 129 (11) (2007) 1465–1475, https://doi.org/10.1115/1.2759969.
[19] Z. Lu, S. Narayanan, E.N. Wang, Modeling of evaporation from nanopores with nonequilibrium and nonlocal effects, Langmuir 31 (36) (2015) 9817–9824, https://doi.org/10.1021/acs.langmuir.5b01700.
[20] S.Q. Cai, A. Bhunia, Characterization of phase change heat and mass transfers in monoporous silicon wick structures, J. Heat Transf. 136 (7) (2014) 072001, https://doi.org/10.1115/1.4027152.
[21] S. Bigham, A. Fazeli, S. Moghaddam, Physics of microstructures enhancement of thin film evaporation heat transfer in microchannels flow boiling, Sci. Rep. 7 (2017), https://doi.org/10.1038/srep44745.
[22] M.A. Hanlon, H.B. Ma, Evaporation heat transfer in sintered porous media, Trans. Am. Soc. Mech. Eng. J. Heat Transf. 125 (4) (2003) 644–652.
[23] S.C. Maroo, J.N. Chung, Negative pressure characteristics of an evaporating meniscus at nanoscale, Nanoscale research letters 6 (1) (2011) 72, https://doi.org/10.1186/1556-276X-6-72.
[24] H. Wang, S.V. Garimella, J.Y. Murthy, Characteristics of an evaporating thin film in a microchannel, Int. J. Heat Mass Transf. 50 (19) (2007) 3933–3942, https://doi.org/10.1016/j.ijheatmasstransfer.2007.01.052.
[25] H. Lee, I. Mudawar, M.M. Hasan, Flow condensation in horizontal tubes, Int. J. Heat Mass Transf. 66 (2013) 31–45, https://doi.org/10.1016/j.ijheatmasstransfer.2013.06.044.
[26] C.R. Kharangate, H. Lee, I. Park, I. Mudawar, Experimental and computational investigation of vertical upflow condensation in a circular tube, Int. J. Heat Mass Transf. 95 (2016) 249–263, https://doi.org/10.1016/j.ijheatmasstransfer.2015.11.010.
[27] M.S. Lee, V. Aute, A. Riaz, R. Radermacher, A review on direct two-phase, phase change flow simulation methods and their applications, 2012.
[28] K.K. Bodla, J.Y. Murthy, S.V. Garimella, Evaporation analysis in sintered wick microstructures, Int. J. Heat Mass Transf. 61 (2013) 729–741, https://doi.org/10.1016/j.ijheatmasstransfer.2013.02.038.
[29] R. Ranjan, J.Y. Murthy, S.V. Garimella, A microscale model for thin-film evaporation in capillary wick structures, Int. J. Heat Mass Transf. 54 (1) (2011) 169–179, https://doi.org/10.1016/j.ijheatmasstransfer.2010.09.037.
[30] R. Ranjan, J.Y. Murthy, S.V. Garimella, Analysis of the wicking and thin-film evaporation characteristics of microstructures, J. Heat Transf. 131 (10) (2009) 101001, https://doi.org/10.1115/1.3160538.
[31] R. Mandel, A. Shooshtari, M. Ohadi, Thin-film evaporation on microgrooved heatsinks, Numer. Heat Transf. Part A: Appl. 71 (2) (2017) 111–127, https://doi.org/10.1080/10407782.2016.1257300.
[32] X. Xu, V.P. Carey, Film evaporation from a micro-grooved surface- an approximate heat transfer model and its comparison with experimental data, J. Thermophys. Heat Transf. 4 (4) (1990) 512–520, https://doi.org/10.2514/3.215.
[33] P.C. Stephan, C.A. Busse, Analysis of the heat transfer coefficient of grooved heat pipe evaporator walls, Int. J. Heat Mass Transf. 35 (2) (1992) 383–391, https://doi.org/10.1016/0017-9310(92)90276-X.
[34] J.M. Ha, G.P. Peterson, The interline heat transfer of evaporating thin films along a micro grooved surface, Transactions-American Society of Mechanical Engineers Journal of Heat Transfer 118 (1996) 747–755.
[35] H.B. Ma, G.P. Peterson, Temperature variation and heat transfer in triangular grooves with an evaporating film, J. Thermophys. Heat Transf. 11 (1) (1997) 90–97.
[36] J.A. Weibel, S.V. Garimella, M.T. North, Characterization of evaporation and boiling from sintered powder wicks fed by capillary action, Int. J. Heat Mass Transf. 53 (19) (2010) 4204–4215, https://doi.org/10.1016/j.ijheatmasstransfer.2010.05.043.

[37] Y. Chen, L.S. Melvin, S. Rodriguez, D. Bell, M.M. Weislogel, Capillary driven flow in micro scale surface structures, Microelectron. Eng. 86 (4) (2009) 1317–1320, https://doi.org/10.1016/j.mee.2009.02.016.
[38] K. Park, K.J. Noh, K.S. Lee, Transport phenomena in the thin-film region of a micro-channel, Int. J. Heat Mass Transf. 46 (13) (2003) 2381–2388, https://doi.org/10.1016/S0017-9310(02)00541-0.
[39] H. Wang, J.Y. Murthy, S.V. Garimella, Transport from a volatile meniscus inside an open microtube, Int. J. Heat Mass Transf. 51 (11) (2008) 3007–3017, https://doi.org/10.1016/j.ijheatmasstransfer.2007.09.011.
[40] M.T. Barako, A. Sood, C. Zhang, J. Wang, T. Kodama, M. Asheghi, X. Zheng, P.V. Braun, K.E. Goodson, Quasi-ballistic electronic thermal conduction in metal inverse Opals, Nano Lett. 16 (4) (2016) 2754–2761, https://doi.org/10.1021/acs.nanolett.6b00468.
[41] Q.N. Pham, M.T. Barako, J. Tice, Y. Won, Microscale Liquid Transport in Polycrystalline Inverse Opals across Grain Boundaries, Sci. Rep. 7 (2017), https://doi.org/10.1038/s41598-017-10791-3.
[42] K.A. Brakke, The surface evolver, Exp. Math. 1 (2) (1992) 141–165, https://doi.org/10.1080/10586458.1992.10504253.
[43] R.W. Schrage, A Theoretical Study of Interphase Mass Transfer, Columbia University Press, 1953.
[44] C.R. Kharangate, I. Mudawar, Review of computational studies on boiling and condensation, Int. J. Heat Mass Transf. 108 (2017) 1164–1196, https://doi.org/10.1016/j.ijheatmasstransfer.2016.12.065.
[45] R. Marek, J. Straub, Analysis of the evaporation coefficient and the condensation coefficient of water, Int. J. Heat Mass Transf. 44 (1) (2001) 39–53, https://doi.org/10.1016/S0017-9310(00)00086-7.
[46] I. Tanasawa, Advances in condensation heat transfer, Adv. Heat Transf. 21 (1991) 55–139, https://doi.org/10.1016/S0065-2717(08)70334-4.
[47] S. Hardt, F. Wondra, Evaporation model for interfacial flows based on a continuum-field representation of the source terms, J. Comput. Phys. 227 (11) (2008) 5871–5895, https://doi.org/10.1016/j.jcp.2008.02.020.
[48] S.V. Patankar, D.B. Spalding, A calculation procedure for heat, mass and momentum transfer in three-dimensional parabolic flows, Int. J. Heat Mass Transf. 15 (10) (1972) 1787–1806, https://doi.org/10.1016/0017-9310(72)90054-3.
[49] R. Peyret (Ed.), Handbook of Computational Fluid Mechanics, Academic Press, 1996.
[50] S. Muzaferija, Computation of free surface flows using interface-tracking and interface-capturing methods, Nonlinear Water Wave Interaction, 1998.
[51] S. Patankar, Numerical Heat Transfer and Fluid Flow, CRC Press, 1980.
[52] J.U. Brackbill, D.B. Kothe, C. Zemach, A continuum method for modeling surface tension, J. Comput. Phys. 100 (2) (1992) 335–354, https://doi.org/10.1016/0021-9991(92)90240-Y.
[53] J.A. Schonberg, P.C. Wayner, Analytical solution for the integral contact line evaporative heat sink, J. Thermophys. Heat Transf. 6 (1) (1992) 128–134.